Article

Ground Deformation Analysis of Bolvadin (W. Turkey) by Means of Multi-Temporal InSAR Techniques and Sentinel-1 Data

Mumin Imamoglu [1,2,*], **Fatih Kahraman** [1], **Ziyadin Cakir** [3] **and Fusun Balik Sanli** [2]

[1] Informatics and Information Security Research Center, TUBITAK, 41470 Gebze, Turkey; fatih.kahraman@tubitak.gov.tr

[2] Department of Geomatic Engineering, Civil Engineering Faculty, Yildiz Technical University, 34220 Istanbul, Turkey; fbalik@yildiz.edu.tr

[3] Department of Geological Engineering, Istanbul Technical University, 34469 Istanbul, Turkey; ziyadin.cakir@itu.edu.tr

[*] Correspondence: mumin.imamoglu@tubitak.gov.tr; Tel.: +90-262-675-3279

check for updates

Abstract: Surface deformations were observed in Bolvadin, located in the province of Afyon (western Turkey) in the last decade which occurred without any destructive earthquakes. In this study, ground deformation of the Bolvadin region is analyzed by means of multi-temporal interferometric synthetic aperture radar (InSAR) technique with Sentinel-1 synthetic aperture radar (SAR) data. Sentinel-1 data acquired in ascending and descending orbits between October 2014 and October 2018 are processed with the Sentinel Application Platform (SNAP) and Stanford Method for Persistent Scatterers (StaMPS) open source software tools. Deformation velocity maps and line-of-sight (LOS) displacement time series are produced and compared with geology, groundwater level and the water surface area of Eber Lake nearby. Deformation velocity maps reveal significant subsidence in most of the town and surrounding regions, which is confirmed by field observations that show severe damage to the settlements and infrastructure of the town. The most severe subsidence is observed to be in the southern part of Bolvadin with rates up to 35 mm/year, which is characterized by the presence of soft alluvial deposits. Composed of slope debris/talus and conglomerate, the northeastern part of the deforming region experiences a relatively lower rate of subsidence. A strong correlation between LOS displacement time series and groundwater level exists both in the short and long term. Moreover, short term variations in LOS displacement time series also show high similarity with seasonal variations in the water surface area of Eber Lake located a few km southeast of the town. We conclude that the primary cause of subsidence is most probably the overexploitation of groundwater and hydrological changes because of (1) the strong correlation of subsidence with lithological units, (2) the similarity between deformation rate and groundwater level changes, (3) the correspondence of seasonal variations in water surface area and short-term deformation rate oscillations, and (4) the absence of InSAR velocity contrast across the active faults.

Keywords: multi-temporal InSAR; time series analysis; sentinel-1; land subsidence; Bolvadin

1. Introduction

Land subsidence is a common geological hazard that affects many regions in the world. Depending on the nature of the region and the man-made activities around it, subsidence phenomena may be triggered by anthropogenic activities such as excessive use of groundwater, mining activities and underground construction or by natural processes such as tectonic movements [1]. Land subsidence may result in infrastructure damage, ground surface ruptures, increasing flood risk and adverse

socio-economic impact in the community [2,3]. Therefore, detecting spatial extent of the deformation pattern and monitoring its temporal evolution is crucial to determine the primary cause of subsidence and conduct preventive activities accordingly to mitigate the negative effects [4].

Over the last two decades, Bolvadin in the province of Afyon (central west of Turkey) has been severely affected by ground deformation such as subsidence, fracturing and fissuring causing severe damage to the settlements and infrastructure. A field study to the region was organized on 12 and 13 February 2019 to observe such deformations in place. Previously reported deformation regions [5] and other potentially damaged areas were visited. Some of the observed surface deformations and their reflections on the buildings are shown in Figure 1a–f. The visited regions and the location of each photograph taken are shown in Figure 2b. Fractures and fissures are clearly seen on the ground in the regions *a* and *c* Although repaving has removed the effects of deformation on the roads in the regions *b* and *d*, stone walls and roadside curbs along them reveals the evidence of deformation. No clear surface deformation was observed in the regions *e* and *f*. However, the presence of quite a few cracks and openings on the wall of the buildings were observed.

Figure 1. Ground deformations observed in Bolvadin and their effects on land, roads and structures.
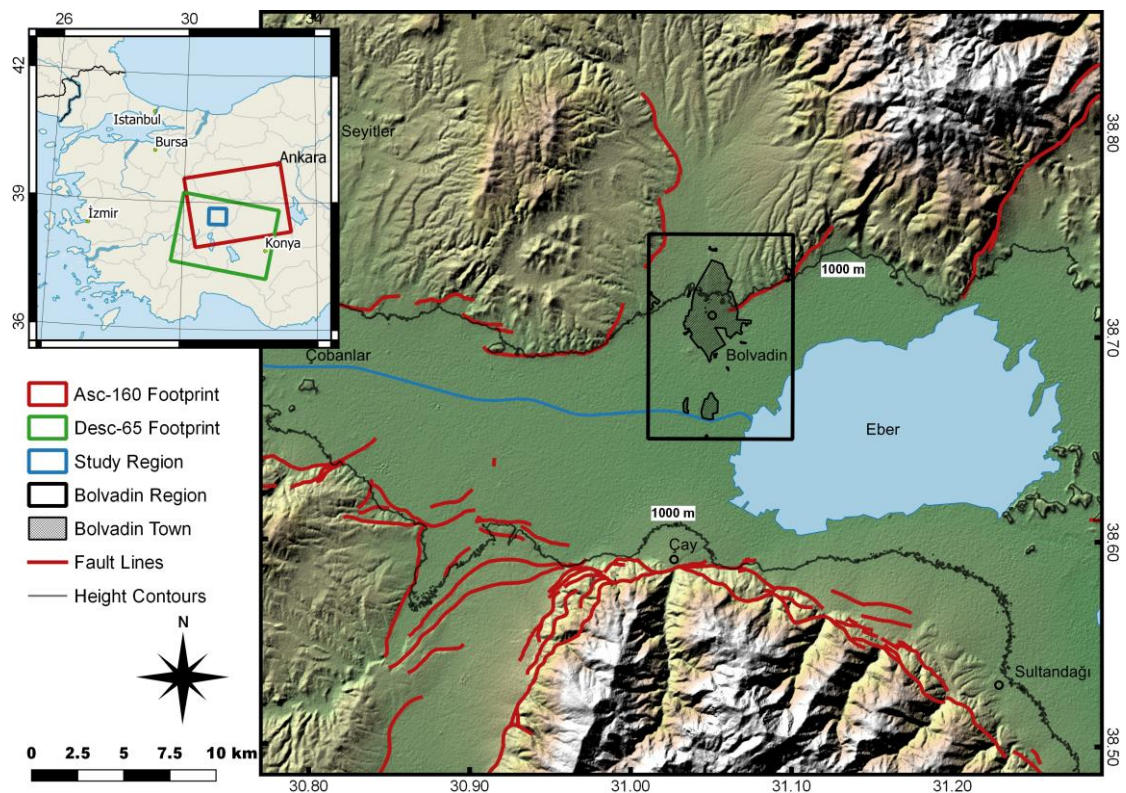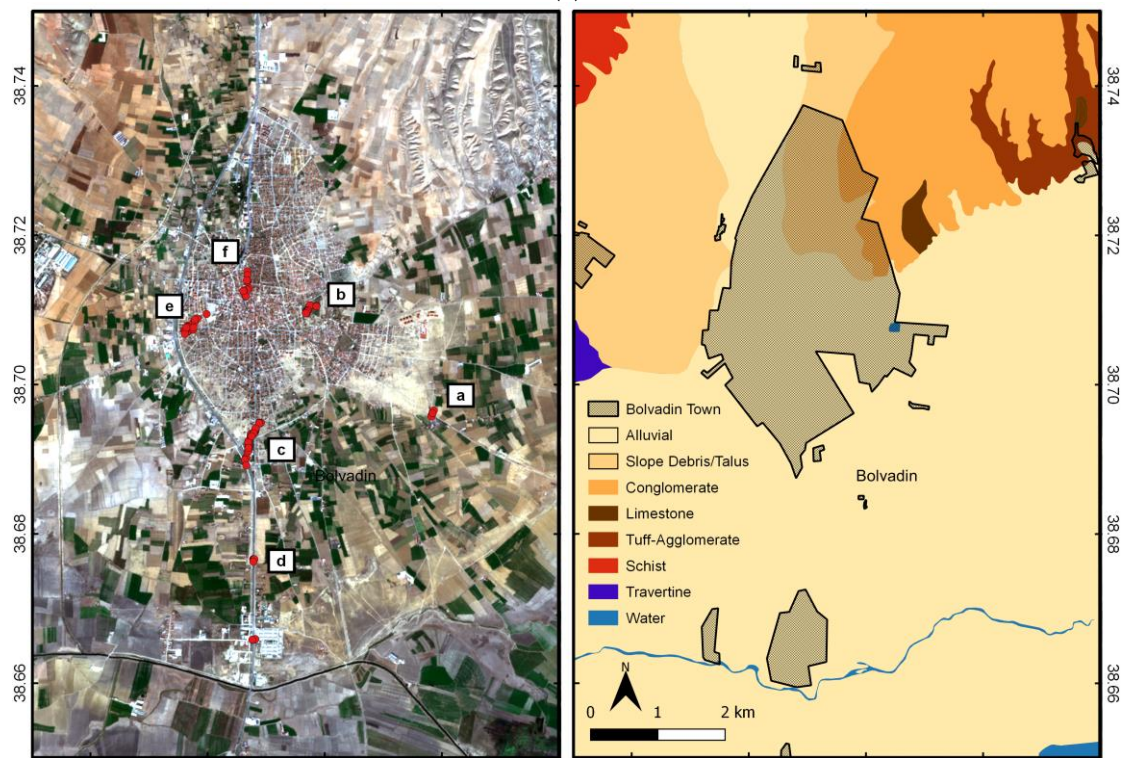
Figure 2. (**a**) Study area (Bolvadin, western Turkey) and surrounding regions with shaded topography, active fault lines and Sentinel-1 footprints. (**b**) Visited regions and location of photographs on Sentinel-2 true color view. (**c**) Geological map of Bolvadin taken from MTA.

This kind of aseismic surface deformation is thought to result from a drastic decrease in ground water table due to excessive pumping or/and drought [5] or creep on nearby active faults [6]. In order to investigate the cause of the surface deformation in the study area, excavations were carried out by [5] in two different areas across fractures that display vertical offsets. Observations on the excavated trench walls reveal that the depths of vertical offsets of 20–30 cm are too shallow (down to 5 m) and offset rate is too high (1.5 to 3 cm/year) to be of tectonic origin, that is, surface creep on active faults buried by the Quaternary alluvium. Consequently, [5] conclude that surface deformations are caused by hydrological changes, not by fault creep or other tectonic motions. However, considering the presence of a complex active fault network [7] and their geodetic observations, [6] suggest that all the surface deformation cannot be explained by ground water table drops only and tectonic creep should also be partly responsible.

In order to examine the seasonal behavior of these deformations, a continuous Global Positioning System (GPS) station was established by [6] in January 2015, and collected data for 2 years. For this specific point, the vertical subsidence rate was found to be 7.1 cm/year. In addition to GPS, a leveling network was established by [8] in August 2016. The network was reoccupied in May 2017. Between 18–24 mm of subsidence was observed during 8 months along 9 profiles [8].

Although ground-based tracking techniques, such as GPS, and leveling measurements provide high-precision measurements, they are obtained at predetermined scares points only. They cannot provide detailed and comprehensive information in the spatial domain. Furthermore, operating these techniques in the field is costly in terms of time and labor [9].

Interferometric synthetic aperture radar (InSAR) is a powerful technique that measures ground surface deformation over a wide area with high precision [10,11]. Satellite-based SAR systems provide very high spatial and high temporal resolution (4–6 days nowadays) over a large area at all weather conditions, day and night. Cost of the InSAR technique, in terms of measurement points per square kilometer, is much lower than other deformation measurement techniques such as GPS and leveling [12]. Advanced InSAR techniques enable time series analysis of multi-temporal SAR data and provide a good set of tools for ground deformation measurements with millimeter precision [13–15]. Previous studies used multi-temporal InSAR technique for analysis of land subsidence due to over exploitation of groundwater [16–20], urban area deformation [21–24], mining region stability [25–27], landslide phenomena [28–30], sinkhole detection [31,32] and seismic events [33,34].

The aim of this study is to understand the mechanism of ground deformation in the study area. To do this, we use multi-temporal InSAR technique with Sentinel-1 TOPSAR data. Sentinel-1 products that were acquired in both ascending and descending orbits between October 2014 and October 2018 were processed using Persistent Scatterer Interferometry (PSI) technique. The velocity fields obtained with PSI are compared with geology, groundwater level and water surface area of Eber Lake nearby.

2. Geographic and Geologic Setting of the Study Area

The study area, namely Bolvadin, is located on the eastern part of the Aegean sub-region of Turkey. Bolvadin is the largest town in the province of Afyon with a population of over 30 thousand. It is built on a wide fertile plain between Sultandağ and Emirdağ mountains on the Aegean coast. The plain is a rich agricultural and farming area watered by the river Akarçay and Lake Eber. Eber Lake is an important water source for the region, positively affecting economic and agricultural activities. However, the water surface area of Eber Lake varies from year to year due to the intense use of water in irrigated agricultural areas, climatic changes and newly built dams in the region [35–37]. Historically, groundwater has been the primary source of water for irrigation and industrial use in the Bolvadin Region. Due to the soft alluvial sediments surrounding the Akarçay River and Lake Eber, many subsidence phenomena affect the area, making it potentially dangerous for civil infrastructures for the study area [5,6].

Bolvadin is located in the middle part of the Afyon-Akşehir Graben system (Figure 2), where the tectonic formation is extremely complex with frequent seismic events [6,7]. In this work, the active

fault database for Afyon-Bolvadin (Figure 2) was taken from the renewed active fault map of Turkey prepared by [7] under the establishment of the Geological Research Department of General Directorate of Mineral Research and Exploration (MTA) of Turkey.

3. Materials and Methods

3.1. Sentinel-1 Dataset

Sentinel-1 is a twin satellite constellation that carries synthetic aperture radar (SAR) sensors operating at C-band (~5.6 cm wavelength) under Copernicus Programme coordinated and managed by the European Space Agency (ESA). Sentinel-1 products are distributed by the Copernicus program under free and open data policy. Sentinel-1 A and Sentinel-1 B together have imaging capability of the same region every 6 days at all weather conditions, day and night. Six-day repeat cycle is quite a good temporal resolution for land monitoring services.

The study area is analyzed for ground surface deformation using Sentinel-1 SAR images within the time period between October 2014 and October 2018. Sentinel-1 A covers the study region from the beginning of the analysis period and Sentinel-1 B starting from October 2016 at ascending track 160 and at descending track 65 as shown in Figure 2a. With the launch of Sentinel-1 B in mid 2016, temporal resolution increased at the second half of the analysis period from 12 days to 6 days. A total of 366 (183 ascending and 183 descending) products acquired in TOPSAR Interferometric Wide (IW) Swath Mode in Single Look Complex (SLC) format are processed independently for each track. The single master image is selected for each dataset separately by considering temporal and geometric baselines of the Sentinel-1 A/B products as displayed in Figure 3. Mean incidence angle of the study area is about 35° for ascending dataset and is around 40.5° for descending dataset.
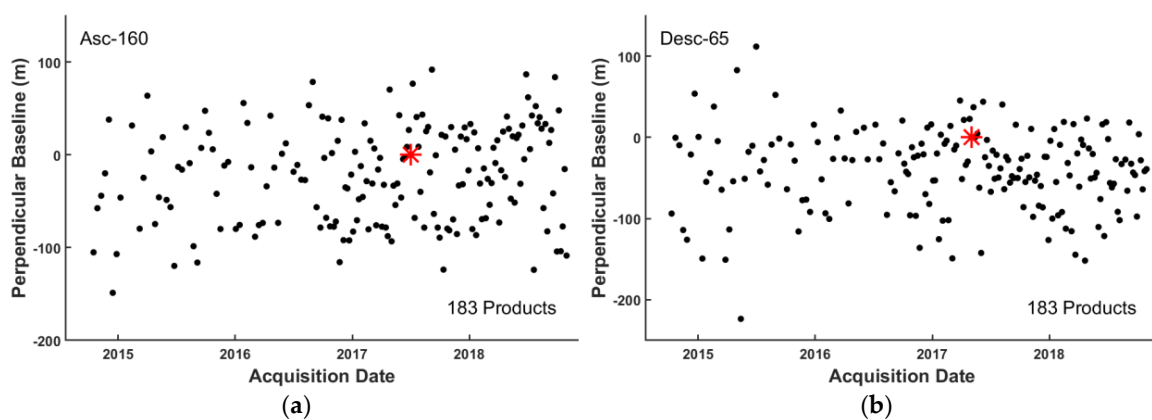

Figure 3. Baseline plot for Sentinel 1 data. Red star represents the master image of all the pairs. (**a**) Asc. track 160, master image date is 5 May, 2017. (**b**) Desc. track 65, master image date is 2 July, 2017.

3.2. Multi-Temporal InSAR Processing

Ground deformation in Bolvadin is analyzed using the PSI technique. Instead of analyzing the whole image, only persistent scatterers (PS) points which are stable over time are analyzed. The main processing steps of PSI consist of interferogram generation, multi-temporal persistent scatterers (PS) processing and removal of atmospheric phase screen (APS) [14]. The processing of each main block is carried out as suggested in [21]. Single master interferograms are generated using Sentinel Application Platform (SNAP, version 6.0) [38]. Initially, data acquired before March 2015 are corrected for Elevation Antenna Pattern (EAP) to obtain appropriate interferograms. EAP used for Sentinel-1 data upgraded to correct the EAP phase in addition to the EAP gain in March 2015. It is reported that this change may cause range varying phase offset while generating interferogram with products acquired before and after [39]. After proper sub-swath and burst selection, all Sentinel-1 slave images are coregistered to a master image with Sentinel-1 Back Geocoding operator using orbit files [40] and digital elevation

model (DEM). Then, interferograms are formed and the topographic phase component is removed. Shuttle Radar Topography Mission (SRTM) [41] with 1 arc-second (~30 m pixel size) DEM is used for the coregistration and for topographic phase removal from the interferometric phase. VV polarization bands are processed since co-polarized bands achieve higher coherency.

The stack of interferograms is passed to the next stage for time series analysis. The Stanford Method for Persistent Scatterers (StaMPS, version 4.1-beta) software package [13,42] is used for selection of PS points within the stack of interferograms and for multi-temporal processing of them. Candidate PS points are initially selected by using the amplitude dispersion index originally proposed by [43] with a relatively higher threshold. Then, spatially-correlated terms are estimated using phase analysis and subtracted from the interferometric phase to obtain more stable PS points that not only depend on signal intensity but also phase stability. In the last stage, the Toolbox for Reducing Atmospheric InSAR Noise (TRAIN) [44] is used to remove atmospheric phase screen. The ERA-I global weather model is used to compute tropospheric phase effects caused by temperature, pressure and humidity variations. Lastly, tropospheric phase delays for each acquisition date are removed from the interferometric phase to obtain the final deformation signal.

4. Results

4.1. Multi-Temporal InSAR Results

As a result of multi-temporal InSAR analysis, two main products are produced; (1) mean deformation velocity maps in line-of-sight (LOS) direction, and (2) time-series of displacements for measurement points that are provided in the following subsections.

4.1.1. Mean Velocity Maps

The mean deformation velocity maps obtained in LOS by multi-temporal analysis of ascending and descending datasets within the time period of October 2014 and October 2018 are shown in Figure 4. All measurement values are relative to a common reference point that is considered to be stable over the entire time period. Warm colors (negative values) highlight displacement that occurred away from the sensor while cold colors (positive values) show movement towards the sensor. Although results are displayed in the range of ± 25 mm/year for visualization purposes, larger displacement rates are present at some locations. The velocity maps of the entire study area in Figure 4a,b show that subsidence is taking place not only in the town of Bolvadin, but also in almost all parts of the Afyon-Akşehir Graben, including the surroundings of Çay, Çobanlar and Sultandağı towns. The majority of the PS points is found to be around the urbanized area. There are almost no measurement points over agricultural areas located around the settlement since great variations in the farmlands are expected in such a long analysis period. However, it is quite clear that the entire graben is exposed to severe subsidence. Figure 4c,d provides mean velocity maps focused on the Bolvadin region. Ascending and descending velocity maps show quite a similar deformation pattern and rates at most of Bolvadin, which is a sign of pure vertical movement. However, there are some areas like the southern part of the city that LOS deformation is different for ascending and descending dataset. That might be an indication of horizontal movement. For that reason, further processing and decomposition of LOS displacement into vertical and horizontal components is required for easier interpretation of movement.

Only the projection of the actual displacement in the LOS direction can be detected by the SAR sensors. Another limitation of deformation measurement is the low sensitivity of SAR sensors to displacement occurred in the N-S direction [45]. In order to obtain 3D movement component, at least 3 different measurements are required obtained by different acquisition geometry. However, the N-S component can be neglected due to the low sensitivity of SAR sensors along that direction. Finally, availability of images obtained at ascending and descending acquisition geometry is enough to calculate vertical and horizontal (E-W) displacement components. Using the same decomposition method outlined in [46] with neglecting the N-S component, vertical and E-W horizontal mean deformation

velocity maps are obtained for the Bolvadin region (Figure 5). In almost every region of Bolvadin, varying rates of subsidence are observed. The maximum vertical subsidence is observed to be around 35 mm/year in the southern part of Bolvadin. North and north-east parts shows relatively smaller deformation rate compared to south and south-west of the city. Although horizontal E-W movement is negligible in most regions, relatively small movement is observed in a small area in the west and specific region in the south.
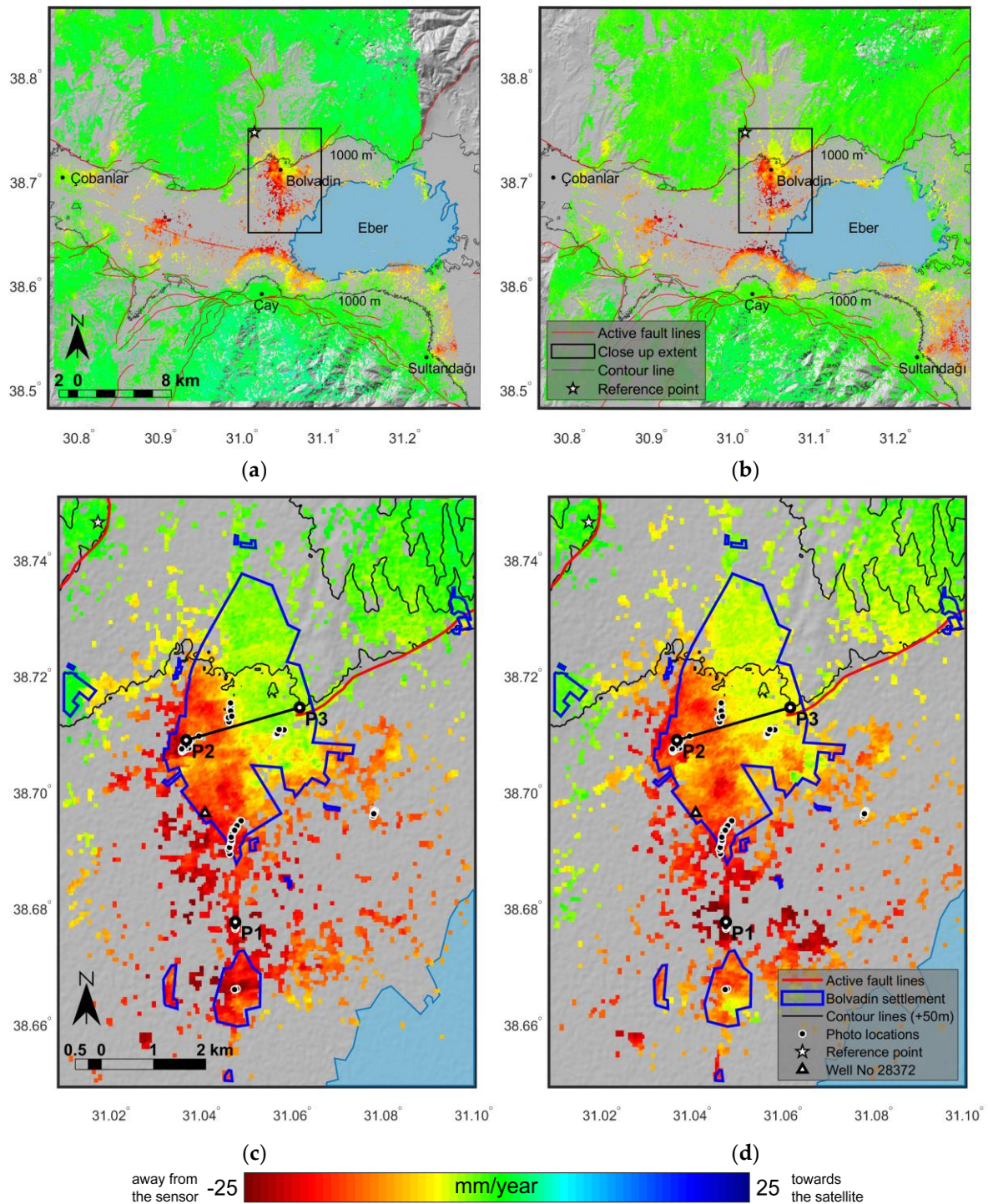

Figure 4. Mean Sentinel LOS velocity maps on ascending track 160 (**a**) and descending track 65 (**b**) in central Afyon-Akşehir graben. Close up view of Bolvadin region on ascending (**c**) and descending (**d**) tracks. P1, P2 and P3 points are used in time series analysis shown in Figure 6.
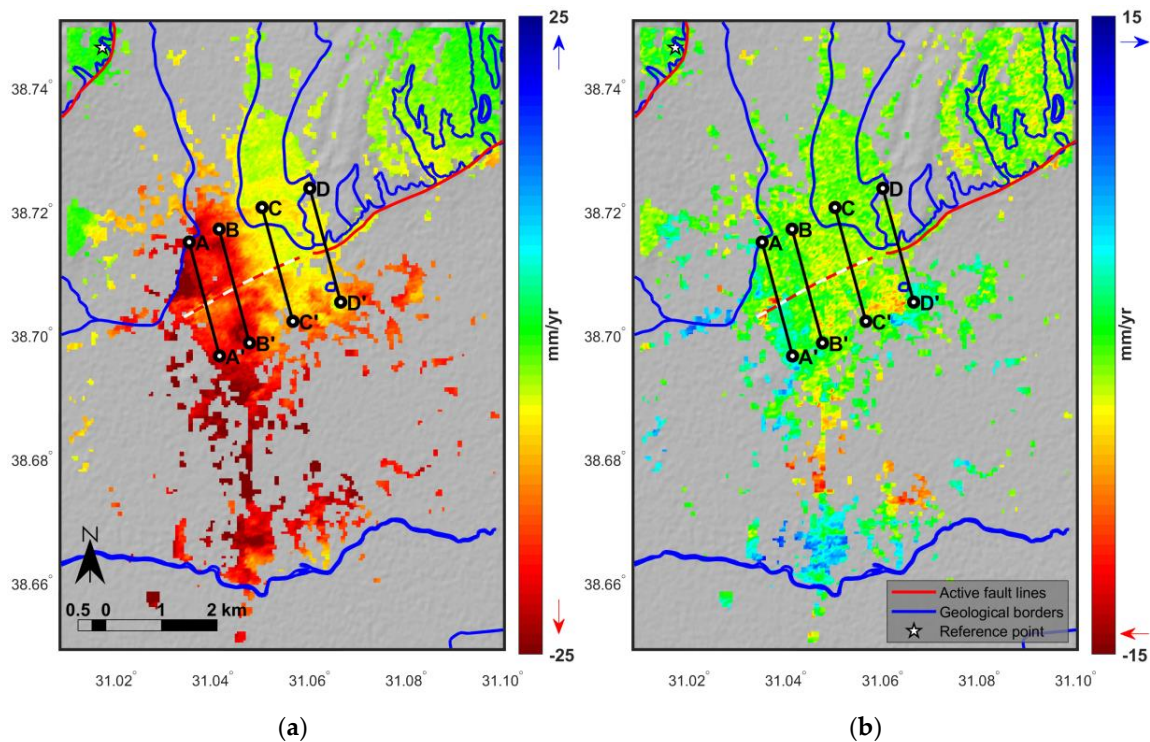
Figure 5. Decomposition of LOS velocities into vertical and horizontal (E-W) components. Dashed red-white lines show possible extension of the Bolvadin fault (solid red line). Deformation rates over profiles AA' to DD' are shown in Figure 8. (**a**) Vertical mean deformation velocity. Warm colors (negative values) represent subsidence. (**b**) Horizontal E-W mean deformation velocity. Warm colors (negative values) represent movements towards west direction and cold colors (positive values) towards east.

4.1.2. Time Series

Three measurement points are selected from different areas of the city that are exposed to different deformation rates. The points are selected as close as possible to the photo locations that were taken during the field study. The locations of the selected points are displayed in Figure 4c,d. The point P1 is selected from the southern part of the town at a location where the most severe subsidence is observed. P2 and P3 points are selected from two different regions that show different subsidence rates. The point P2 is located in the western part of the city, and the point P3 is located in the eastern part of the city where relatively low deformation rates are observed. Figure 6a–f show ascending and descending LOS time-series at all selected points, respectively. The mean of all points on a radius of 100 m is calculated as a LOS displacement. The original displacement values are shown together with the linear fit result.

In the long term, both datasets indicate secular movements away from the sensor at all points, which is an indication of subsidence. While observed cumulative displacement at P1 in ascending LOS is approximately 8 cm, it is about 12 cm in the descending dataset. The difference of cumulative measured displacement in LOS between the ascending and descending datasets can be explained with the existence of horizontal movements in that region as shown in Figure 5b. LOS cumulative displacements at P2 decrease to about 7 cm for both datasets. P3 is a relatively more stable point that shows about 2 cm of LOS cumulative displacement in both datasets. Similar displacement values and patterns at P1 and P2 are indicative of pure vertical deformation. Additionally, short-term oscillations are observed in all selected points. As the general deformation trend decreases, the amount of oscillation decreases from P1 to P3. Effects of seasonal variations on oscillation will be analyzed in details in the following subsections.
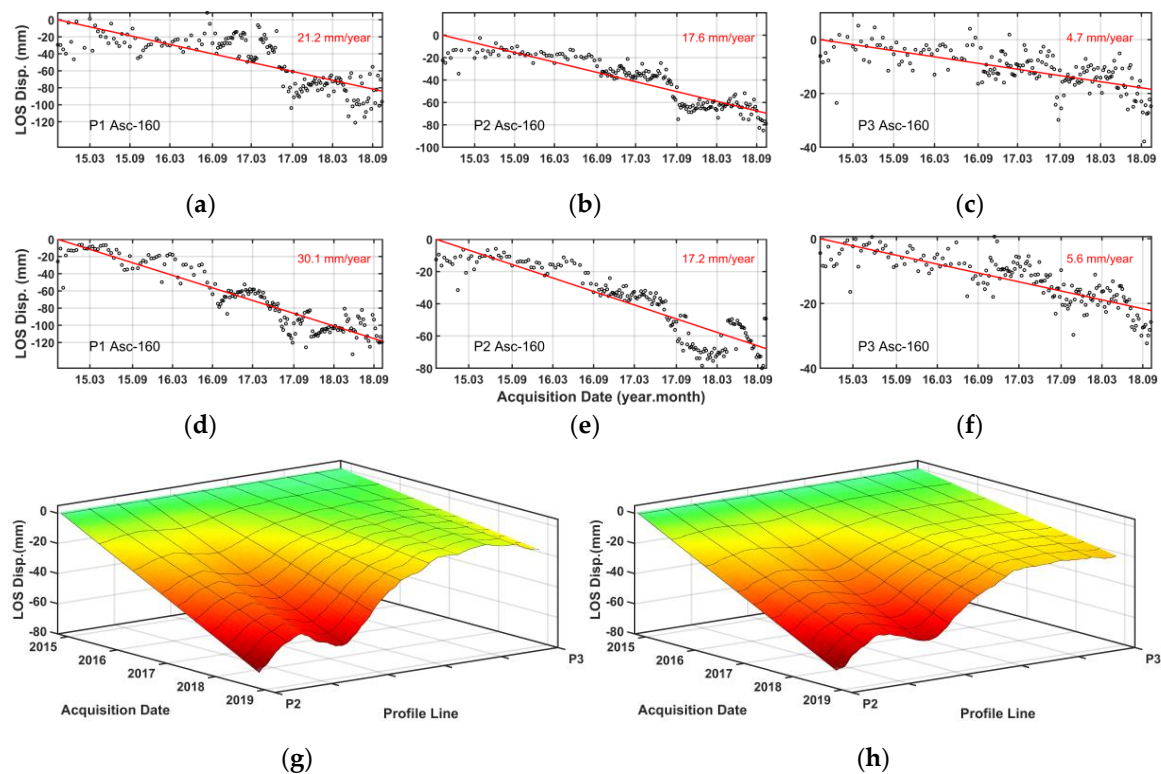
Figure 6. LOS displacement time series at selected points are shown together with linear fit for Asc.-160 (**a**) P1 (**b**) P2 (**c**) P3 and Desc.-65 (**d**) P1 (**e**) P2 (**f**) P3. Linear fit of LOS displacement time series on the profile between points P2 and P3 are displayed-for (**g**) Asc.-160 and (**h**) Des.-65, tracks. Points and profile locations are shown in Figure 4c,d.

In order to illustrate how the rate of deformation changes between two different regions during the analysis period, all displacement time series along the profile line between the points P2 and P3 are combined. For the sake of simplicity, only the linear approximations of LOS displacements are shown in Figure 6c,d for ascending and descending datasets. Obviously, all measurement points over the P2-P3 line are exposed to subsidence. However, there has been an increase in subsidence over the years from point P3 to P2. While about 2 cm of cumulative displacement is observed at the point P3, there is approximately 7 cm of subsidence at the point P2 in LOS direction. Cumulative displacement values in LOS correlate with ascending and descending dataset since negligible horizontal E-W movement is observed in the region.

4.2. Comparison with Lithology

As previously stated, Bolvadin is located in the central part of the Afyon-Akşehir Graben system, and mainly characterized by the existence of alluvial sediments. The lithological units in the north and the north-east area of Bolvadin are composed of slope debris/talus and conglomerates. The outer regions of the town also contain limestones and schists. Mean deformation velocity maps and geological boundaries provided in Figure 5 show a clear correlation with alluvial sediments and high deformation rates that exist in the southern and western part of the city. The LOS cumulative displacement time series of points P1 and P2 are selected from these regions and results are shown in Figure 6. Slope debris/and conglomerate are made of coarse grains and blocks and thus are less deformable sediments where a decrease in deformation rate could be observed as in the case of the point P3. Displacement time series along the profile line between points P2 and P3 (Figure 6c,d) shows a clear distinction in which the rate of deformation changes between alluvial sediments and slope debris/talus. The most stable area with almost zero deformation velocity is in the north-western part of the region where schist formation is observed. The reference point is selected from that stable region

and all other measurement points are updated accordingly. Therefore, the velocity fields are relative to the reference point in this region.

The correlation between geological units and vertical and horizontal (E-W) deformation can be seen in Figure 7. The mean, standard deviation, and minimum and maximum deformation rates of each geological unit are calculated. As expected, while most of the deformation occurs in soft alluvium deposits, the old geological formations are much less affected. The maximum subsidence rate is observed to be around 35 mm/year in the alluvial deposits in the southern part of Bolvadin. While average subsidence rate is about 15 mm/year in alluvium deposits, other geological units exhibit very little or no deformation. Although mean subsidence rate of slope debris/talus is about 7 mm/year, the maximum subsidence rate reaches up to 25 mm/year. On the other hand, mean horizontal (E-W) deformation velocity is almost zero for all geological units. However, especially in alluvial sediments, both east and west movements are observed in some regions with the maximum rate about 12 mm/year.
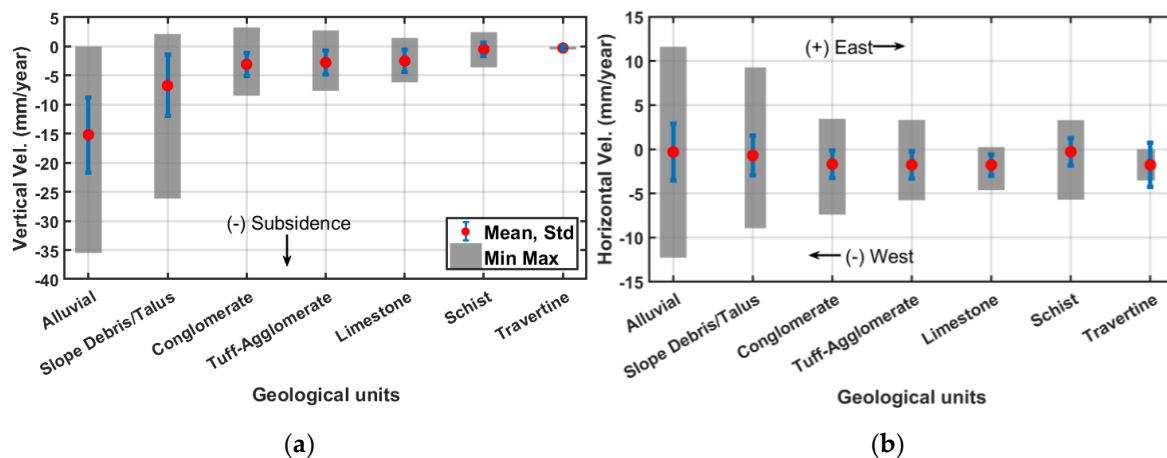

Figure 7. Relationship between geological units in the Bolvadin region and (**a**) Vertical deformation velocity, (**b**) Horizontal (E-W) deformation velocity. The mean (red dots), standard deviation (blue line), minimum and maximum (bold gray) values of deformation velocity are shown for each geological unit.

4.3. Comparison with Water Surface Area of Eber Lake

Study [37] claims that the surface area of Lake Eber grew by 2.30% between 1990–2016. However, it has recently been reported by several newspapers that the lake has almost dried up as of October 2018 [47,48]. Understanding groundwater–surface water relation is a difficult problem and has received much attention in the literature. Several recent studies are focused on this issue. Researchers of [49] studied interactions between lakes/reservoirs/wetlands with groundwater while [50] presented a comprehensive survey of groundwater and surface-water relation, [51] reported the detailed case study about the correlation between groundwater and the surface-water level of Lake Nasser. Nevertheless, it is claimed by [52] that Eber Lake does not directly interact with groundwater and groundwater level changes do not affect the water level. The lake is thought by [35] to be mainly fed by rainfall and spring water coming from the Akarçay and Sultan Mountains. However, it is suggested by [50] that precipitation is also one of the main sources of groundwater level. Thus, both Eber Lake water surface and groundwater level are affected by climate and precipitation.

The water surface area of Eber Lake varies over the years due to different amounts of precipitation, evaporation, irrigation, pumping and surface flow [35–37]. All meteorological information in Turkey, including rainfall data, is collected by The Turkish State Meteorological Service (TSMS). The monthly average precipitation data for the province of Afyon, which was calculated using the data obtained in period 1929–2018, was published on the TSMS website [53]. On the other hand, the Lake of Eber is one of the 5000 lakes on the Earth which is constantly monitored by the Bluedot Observatory. The water surface area of the lake is analyzed using multispectral Sentinel-2 optical data between July 2015 and November 2018 [54]. The percentage of water surface area relative to normal lake boundaries is

calculated for each Sentinel-2 data. The monthly average rainfall data (mm) and monthly average water surface area (%) of Eber Lake are shown together in Figure 8a. There is quite a good correlation between monthly rainfall data and water surface area of the lake, which shows that precipitation is one of the main sources of Eber Lake. Both rainfall data and water surface area reach to a maximum value in spring and decreases to the minimum level at the end of summer period. Precipitation is one of the main reasons affecting the water surface area of Eber Lake, but another possible reason might be irrigation. One of the water sources of agricultural areas is definitely Eber Lake and surrounding rivers that directly feed Eber Lake. Therefore, extensive use of water in agriculture during the summer period is another important factor in reducing the water surface area to a minimum level.
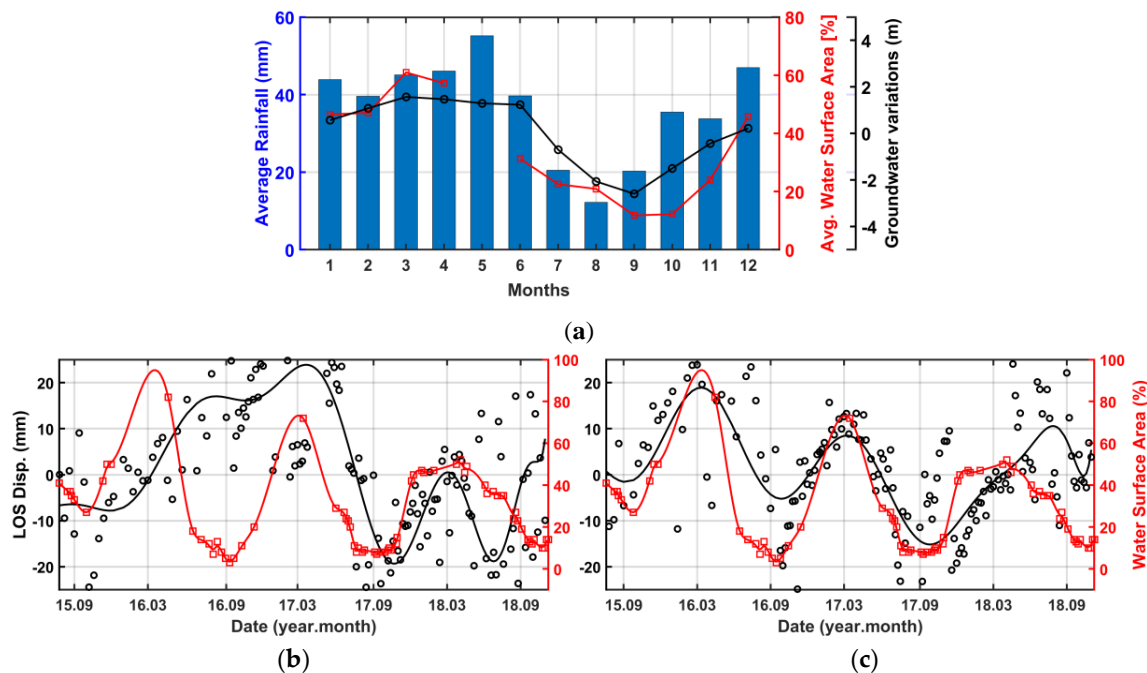

Figure 8. (**a**) Monthly average rainfall (mm) in Afyon city vs. monthly average water surface area of Eber Lake and groundwater level changes after the long-term decline trend line is removed. After removal of long-term subsidence trend, P1 LOS displacement is shown together with areal water surface coverage (%) of Eber Lake for (**b**) Asc.-160. (**c**) Des.-65 tracks. Both original data and polynomial approximation are shown in the plot.

InSAR LOS displacement time series measurements of the point P1 for both datasets are compared with water surface area of Lake Eber obtained from Bluedot Observatory in Figure 8b,c. The long-term linear subsidence trend is subtracted from the LOS time series and then a polynomial (15th order) model is fit to each time series. There are deficiencies in surface water surface area data, especially in winter seasons due to lack of cloudless optical data. Therefore, missing parts are filled again with a polynomial approximation. It can be observed that the water surface area of the lake falls to its lowest level at the end of the summer period and reaches its highest level in spring. When the water level is minimal, the surface area of the lake falls below 10% of the natural lake boundaries and even close to zero in 2016. The water surface area starts increasing in autumn and reaches its highest level in spring. However, it should also be noted that there is a long term decrease at the highest level of lake surface area. As for the comparison with LOS displacements, there is a clear indication of temporal patterns affected by seasonal water surface area changes in the descending data set. Compared to the descending data set, the ascending dataset shows relatively less correlation with seasonal patterns.

4.4. Comparison with Groundwater Level

Variations in the groundwater level may trigger ground surface deformation for multiple reasons [17]. One of the most effective reasons is that the decrease in groundwater level causes changes in the stress level on deformable soils that result in subsidence. Therefore, the groundwater level in the region is an important factor that may trigger ground surface deformation. Groundwater level data are obtained from the Directorate of Turkish State Hydraulic Work. Location of the well no 28372 is shown in Figure 4c,d. Cumulative ground surface deformation measured in LOS is compared with groundwater level in Figure 9 for ascending and descending datasets, respectively. There is quite a good correlation between groundwater level changes and LOS deformation trends both in long term and short term. In the long term, both data show a generic decline trend due to overexploitation of groundwater. In the short term, with the effect of rainfall and irrigation, seasonal changes are observed.
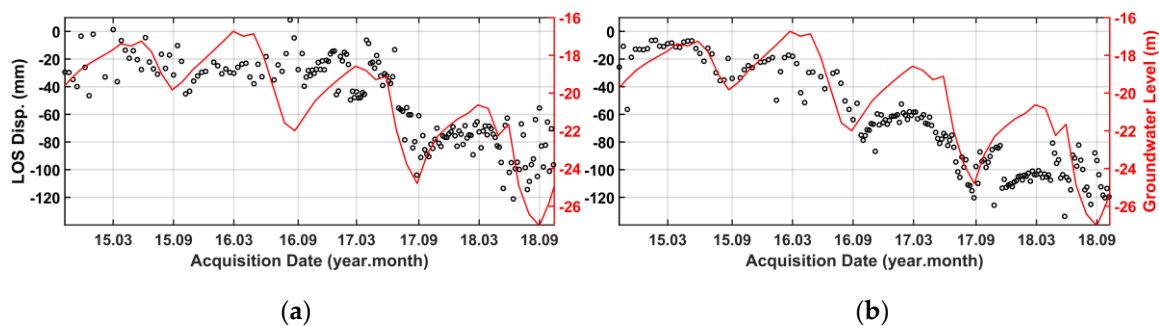

(**a**)   (**b**)

Figure 9. LOS displacement time series of point P1 vs. temporal evolution of groundwater level at well no 28372 are shown together for (**a**) Asc.-160. (**b**) Des.-65 tracks. Location of the well is shown in Figure 4c,d.

Irrigation and precipitation are two main reasons for groundwater variations. Groundwater has been the primary source of water for irrigation in the region. Extensive use of groundwater for agriculture results in the decrease of groundwater level throughout the years. It can be observed in Figure 9 that there is a generic decline trend in groundwater levels that causes subsidence phenomenon in the long term. Together with irrigation, another important factor of groundwater level variation is the rainfall. The long-term decline trend line is removed from the groundwater level and compared with monthly average rainfall in Figure 8a. As precipitation increases in spring, the groundwater level also increases. As a result of the groundwater level increase, short term uplift is observed on the ground. Towards the end of the summer, the opposite effect is observed with decreasing rainfall. Hence, subsidence starts to be effective in the region. The increase in irrigation in the summer period also contributes to the aforementioned process.

5. Discussion

Several studies have been carried out to investigate the causes of surface deformations in the Bolvadin region, [5,6,8]. There is no debate about the primary cause of surface deformation which is thought to be hydrological changes. However, there are different approaches about the effects of the tectonics. While [5] do not accept the effect of tectonic movements on ground surface deformations, [6] suggest that even though there was no destructive earthquake, intensive micro-seismic activity, and related reasons may have affected the formation of surface deformations. Ground level measurements with GPS and leveling show the rate of deformation on specific points around faults and fissures. Although these kinds of techniques provide precise measurements, they are limited to discrete locations.

In this study, the ground deformation analysis of the entire Bolvadin region is performed by using the multi-temporal InSAR technique with Sentinel-1 TOPSAR data. Initially, LOS deformation velocity maps are produced for ascending and descending tracks as shown in Figure 4. Later on, vertical and horizontal (E-W) displacements are generated by decomposition of ascending and descending LOS

velocities, Figure 5. It is quite clear that the southern and western parts of the city have been exposed to vertical deformation as a whole. Towards the south, the subsidence rate increases and reaches up to 35 mm/year, most probably due to increasing groundwater extraction in the agricultural fields and thickening of the alluvial deposits. Deformation rate highly correlates with the lithological units of the region as most of the vertical deformations is observed in soft alluvial sediments and approaches to zero as we move away from alluvial sediments.

In order to evaluate the possible effects of the Bolvadin fault entering the city from the east, deformation rates are examined with profiles of vertical velocity field across the fault. Figure 5 shows four profiles that perpendicularly cross the fault strike and its probable southwest continuation beneath the alluvium. Vertical and horizontal (E-W) mean deformation velocities over profiles are shown in Figure 10. There is no obvious or consistent vertical or horizontal deformation velocity change across the Bolvadin fault that might be indicative of tectonics origins. However, especially AA′ and BB′ profiles passing through soft alluvium sediments show significant variation across the Bolvadin fault. These asymmetric deformation patterns must be mainly due to the different amount of materials types within alluvial sediments because aseismic slip on the Bolvadin fault is expected to produce subsidence not on the northern side, but on the southern side (i.e., hangingwall) of the fault. The deformation rates of the CC′ and DD′ profiles are more stable in short time periods as they are situated over more compacted lithological units. When the profiles are examined, vertical velocities in the far field away from the Bolvadin fault are in general roughly the same, that is, there is no differential motion (i.e., downthrown of hangingwall southern block) across the fault that might have been caused by creep on a normal fault that dips to the south, implying that the fault has no apparent contribution to the observed subsidence.
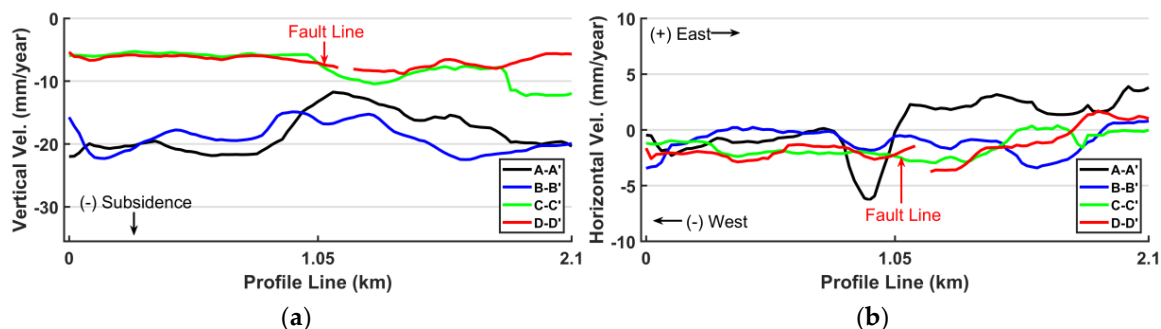

Figure 10. Mean velocities along the profiles AA′-DD′ shown in Figure 5. (**a**) Vertical mean velocity. (**b**) Horizontal (E-W) mean velocity.

We compare water surface area of Eber Lake and LOS displacement time series for ascending and descending orbits. As shown in Figure 8b,c, a clear correlation between the seasonal variation of water surface area of Eber Lake and displacement time series is revealed when the long-term linear subsidence trend is removed from the LOS displacements. There is a lag time between the peak level of the lake water surface area and the displacement time series. It can be observed from the time series of individual points that correlation of LOS displacements with seasonal variation of water surface area increases towards the south of the region. The effect of seasonal change on different regions can also be examined by looking at the local standard deviation of the mean deformation velocity. Statistics provided in Figure 7 include the whole area for each geological unit. In order to observe how seasonal variation affects different regions, additionally, the standard deviations for local regions alone are also calculated. The average standard deviation for the deformation rate increases for both dataset from 0.3 mm/year to 1.7 mm/year as from north to the south. The increase of standard deviation is a direct effect of seasonal variation. Although the water source of Eber Lake has no direct relation with groundwater, both Eber Lake water surface and ground water level are affected by climate and fed by precipitation. Moreover, LOS displacement time series for both datasets are compared with groundwater level changes. There is quite a good correlation between groundwater level changes and

LOS deformation trends both in long term and short term as shown in Figure 9a,b. As a result, the relation of groundwater level and lake water surface area with displacement time series show effects of hydrological changes to deformation.

Correlation of the high deformation rate with soft lithological units of the Bolvadin region, the similarity between deformation rate and groundwater level changes and the high correlation of deformation rate change with seasonal variations in water surface of Eber Lake suggest that subsidence phenomenon might be a direct result of hydrological effects in the region. Besides, mean deformation velocities over the profile lines AA'-DD' suggest that there is no clear spatial evidence about the effects of the Bolvadin fault on deformation. Furthermore, the surface deformations in the a, c regions such as fracturing and fissuring are almost in the south-west north-east direction which is not parallel to the Bolvadin fault. As a result, it is very likely that those surface deformations observed in the region are the consequences of generic deformation trend affecting the whole graben system which is mainly caused by overexploitation of ground water and hydrological changes in the region.

6. Conclusions

We have mapped the ground surface deformation in Bolvadin using Sentinel-1 SAR images on both ascending and descending tracks within the time period of October 2014 and October 2018. As a result of multi-temporal InSAR analysis, two main products are produced: (i) Mean deformation velocity maps, (ii) Time-series of displacements for measurement points. The mean velocity maps show that the town of Bolvadin almost entirely subsides at different rates reaching 35 mm/year. The subsidence is taking place not only in Bolvadin, but also almost in the entire Afyon-Akşehir Graben.

We observe a strong spatial correlation between subsidence and lithology, a high similarity between deformation rate and groundwater level changes, and a temporal correlation between subsidence rate and Eber Lake water surface changes. There is no specific deformation pattern observed around the Bolvadin fault that might continue westward into the city center. As a result, we conclude that the primary cause of surface deformations is the overexploitation of ground waters and hydrological changes that affect the entire basin.

This study is the first step of the project related to the continuous monitoring of land deformation in the country scale using SAR data. The main purpose of this study is to investigate deformation phenomenon in a region-scale and extend our understanding of it to all subsidence regions across the country. Continuous monitoring of deformations throughout the country is crucial for sustainable planning and risk management. Sentinel-1 data show a high potential in the field of near real-time land deformation monitoring with wide coverage and regular data acquisition. This study suggests that the temporal and spatial behaviors of subsidence basins in Turkey can be investigated using Sentinel-1 data and PSI technique. To achieve this, all the processing steps used in this study will be updated to be capable of working on multiple processor stations and computer clusters to handle the enormous workload.

References

1. Strozzi, T.; Wegmüller, U.; Tosi, L.; Bitelli, G.; Spreckels, V. Land subsidence monitoring with differential SAR interferometry. *Photogramm. Eng. Remote Sens.* **2001**, *67*, 1261–1270.

2. Galloway, D.; Jones, D.R.; Ingebritsen, S.E. *Land Subsidence in the United States*; U.S. Department of the Interior, U.S. Geological Survey: Reston, VA, USA, 1999; Volume 1182.

3. Holzer, T.L.; Galloway, D.L. Impacts of land subsidence caused by withdrawal of underground fluids in the united states. *Rev. Eng. Geol.* **2005**, *16*, 87–99.

4. Tomás, R.; Li, Z. Earth observations for geohazards: Present and future challenges. *Remote Sens.* **2017**, *9*, 194. [CrossRef]

5. Demirtaş, R.; Tepeuğur, E. Bolvadin (Afyon) Merkez yerleşim alaninda son 15 yillik dönemde oluşmuş yüzey kiriklarinin oluşum mekanizmasi. In Proceedings of the ATAG-21: Aktif Tektonik Araştırma Grubu Çalıştayı, Afyon, Turkey, 26–28 October 2017.

6. Özkaymak, Ç.; Sözbilir, H.; Tiryakioğlu, İ.; Baybura, T. Bolvadin'de (Afyon-Akşehir Grabeni, Afyon) Gözlenen Yüzey Deformasyonlarının Jeolojik, Jeomorfolojik ve Jeodezik Analizi. *Türk. Jeol. Bül. Geolog. Bull. Turk.* **2017**, *60*, 169–189. [CrossRef]

7. Emre, Ö.; Duman, T.Y.; Özalp, S.; Olgun, S.; Elmaci, H. 1:250,000 Scale active fault map series of Turkey Afyon (NJ 36-5) quadrangle. In *General Directorate of Mineral Research and Exploration*; (Serial number: 16); General Directorate of Mineral Research and Expansion (MTA): Ankara, Turkey, 2011.

8. Tiryakioğlu, İ.; Uğur, M.A.; Yalçın, M.; Baybura, T.; Yilmaz, M.; Özkaymak, Ç.; Sözbilir, H. Akşehir Simav Fay Sistemindeki Güncel Tektonik Hareketlerinin Izlenmesi: Nivelman Çalişmalari. 4. In Proceedings of the Uluslararası Deprem Mühendisliği ve Sismoloji Konferansı, Eskişehir, Turkey, 11–13 October 2017.

9. Qu, F.; Lu, Z.; Zhang, Q.; Bawden, G.W.; Kim, J.-W.; Zhao, C.; Qu, W. Mapping ground deformation over Houston-Galveston, Texas using multi-temporal InSAR. *Remote Sens. Environ.* **2015**, *169*, 290–306. [CrossRef]

10. Gabriel, A.K.; Goldstein, R.M.; Zebker, H.A. Mapping small elevation changes over large areas: differential radar interferometry. *J. Geophys. Res. Solid Earth* **1989**, *94*, 9183–9191. [CrossRef]

11. Massonnet, D.; Feigl, K. Radar interferometry and its application to changes in the Earth's surface. *Rev. Geophys.* **1998**, *36*, 441–500. [CrossRef]

12. Tomás, R.; Romero, R.; Mulas, J.; Marturià, J.J.; Mallorquí, J.J.; Lopez-Sanchez, J.M.; Duque, S. Radar interferometry techniques for the study of ground subsidence phenomena: a review of practical issues through cases in Spain. *Environ. Earth Sci* **2014**, *71*, 163–181. [CrossRef]

13. Hooper, A.; Bekaert, D.; Spaans, K.; Arıkan, M. Recent advances in SAR interferometry time series analysis for measuring crustal deformation. *Tectonophysics* **2011**, *514*, 1–13. [CrossRef]

14. Osmanoğlu, B.; Sunar, F.; Wdowinski, S.; Cabral-Cano, E. Time series analysis of InSAR data: Methods and trends. *ISPRS J. Photogramm. Remote Sens.* **2015**, *115*, 90–102. [CrossRef]

15. Crosetto, M.; Monserrat, O.; Cuevas-González, M.; Devanthéry, N.; Crippa, B. Persistent scatterer interferometry: A review. *ISPRS J. Photogramm. Remote Sens.* **2016**, *115*, 78–89. [CrossRef]

16. Bell, J.W.; Amelung, F.; Ferretti, A.; Bianchi, M.; Novali, F. Permanent scatterer InSAR reveals seasonal and long-term aquifer-system response to groundwater pumping and artificial recharge. *Water Resour. Res.* **2008**, *44*, 1–18. [CrossRef]

17. Bonì, R.; Herrera, G.; Meisina, C.; Notti, D.; Béjar-Pizarro, M.; Zucca, F.; Gonzàlez, P.J.; Palano, M.; Tomàs, R.; Fernàndez, J.; et al. Twenty-year advanced DIn-SAR analysis of severe land subsidence: The Alto Guadalentín Basin (Spain) case study. *Eng. Geol.* **2015**, *198*, 40–52. [CrossRef]

18. Chen, M.; Tomás, R.; Li, Z.; Motagh, M.; Li, T.; Hu, L.; Gong, H.; Li, X.; Yu, J.; Gong, X. Imaging land subsidence induced by groundwater extraction in Beijing (China) using satellite radar interferometry. *Remote Sens.* **2016**, *8*, 468. [CrossRef]

19. Chaussard, E.; Milillo, P.; Bürgmann, R.; Perissin, D.; Fielding, E.J.; Baker, B. Remote sensing of ground deformation for monitoring groundwater management practices: Application to the Santa Clara Valley During the 2012–2015 California drought. *J. Geophys. Res. Solid Earth* **2017**, *122*, 8566–8582. [CrossRef]

20. Haghighi, M.H.; Motagh, M. Ground surface response to continuous compaction of aquifer system in Tehran, Iran: Results from a long-term multi-sensor InSAR analysis. *Remote Sens. Environ.* **2019**, *221*, 534–550. [CrossRef]

21. Imamoglu, M.; Kahraman, F.; Abdikan, S. Preliminary results of temporal deformation analysis in Istanbul using multi-temporal InSAR with Sentinel-1 SAR data. In Proceedings of the 2018 IEEE International Geoscience and Remote Sensing Symposium (IGARSS), Valencia, Spain, 22–27 July 2018.

22. Aslan, G.; Cakır, Z.; Ergintav, S.; Lasserre, C.; Renard, F. Analysis of secular ground motions in Istanbul from a long-term InSAR time-series (1992–2017). *Remote Sens.* **2018**, *10*, 408. [CrossRef]

23. Bonì, R.; Bosino, A.; Meisina, C.; Novellino, A.; Bateson, L.; McCormack, H. A methodology to detect and characterize uplift phenomena in urban areas using Sentinel-1 data. *Remote Sens.* **2018**, *10*, 607. [CrossRef]

24. Erten, E.; Rossi, C. The worsening impacts of land reclamation assessed with Sentinel-1: The Rize (Turkey) test case. *Int. J. Appl. Earth Obs. Geoinf.* **2019**, *74*, 57–64. [CrossRef]

25. Abdikan, S.; Arıkan, M.; Şanlı, F.B.; Çakir, Z. Monitoring of coal mining subsidence in peri-urban area of Zongundak city (NW Turkey) with persistent scatterer interferometry using ALOS-PALSAR. *Environ. Earth Sci.* **2014**, *71*, 4081–4089. [CrossRef]

26. Czikhardt, R.; Papco, J.; Bakon, M.; Liscak, P.; Ondrejka, P.; Zlocha, M. Ground stability monitoring of undermined and landslide prone areas by means of sentinel-1 multi-temporal InSAR, case study from Slovakia. *Geosciences* **2017**, *7*, 87. [CrossRef]

27. Carlà, T.; Farina, P.; Intrieri, E.; Ketizmen, H.; Casagli, N. Integration of ground-based radar and satellite InSAR data for the analysis of an unexpected slope failure in an open-pit mine. *Eng. Geol.* **2018**, *235*, 39–52. [CrossRef]

28. Béjar-Pizarro, M.; Notti, D.; Mateos, R.M.; Ezquerro, P.; Centolanza, G.; Herrera, G.; Bru, G.; Sanabria, M.; Solari, L.; Duro, J.; et al. Mapping vulnerable urban areas affected by slow-moving landslides using sentinel-1 InSAR data. *Remote Sens.* **2017**, *9*, 876. [CrossRef]

29. Intrieri, E.; Raspini, F.; Fumagalli, A.; Lu, P.; Del Conte, S.; Farina, P.; Allievi, J.; Ferretti, A.; Casagli, N. The maoxian landslide as seen from space: Detecting precursors of failure with sentinel-1 data. *Landslides* **2018**, *15*, 123–133. [CrossRef]

30. Bayer, B.; Simoni, A.; Mulas, M.; Corsini, A.; Schmidt, D. Deformation responses of slow moving landslides to seasonal rainfall in the Northern Apennines, measured by InSAR. *Geomorphology* **2018**, *308*, 293–306. [CrossRef]

31. Kim, J.W.; Lu, Z.; Degrandpre, K. Ongoing deformation of sinkholes in Wink, Texas, observed by time-series Sentinel-1a SAR interferometry (preliminary results). *Remote Sens.* **2016**, *8*, 313. [CrossRef]

32. Caló, F.; Notti, D.; Galve, J.P.; Abdikan, S.; Görüm, T.; Pepe, A.; Balik Şanli, F. DInSAR-based detection of land subsidence and correlation with groundwater depletion in Konya Plain, Turkey. *Remote Sens.* **2017**, *9*, 83. [CrossRef]

33. Hussain, E.; Wright, T.J.; Walters, R.J.; Bekaert, D.P.; Lloyd, R.; Hooper, A. Constant strain accumulation rate between major earthquakes on the North Anatolian Fault. *Nat. Commun.* **2018**, *9*, 1392. [CrossRef]

34. Liu, C.; Ji, L.; Zhu, L.; Zhao, C. InSAR-constrained interseismic deformation and potential seismogenic asperities on the Altyn Tagh Fault at 91.5–95° E, Northern Tibetan Plateau. *Remote Sens.* **2018**, *10*, 943. [CrossRef]

35. Sener, E.; Davraz, A.; Sener, S. Investigation of Aksehir and Eber Lakes (SW Turkey) coastline change with multitemporal satellite images. *Water Resour. Manag.* **2010**, *24*, 727–745. [CrossRef]

36. Yıldırım, Ü.; Erdoğan, S.; Uysal, M. Changes in the coastline and water level of the Akşehir and Eber Lakes between 1975 and 2009. *Water Resour. Manag.* **2011**, *25*, 941–962. [CrossRef]

37. Köle, M.M.; Ataol, M.; Erkal, T. Eber ve Akşehir Gölleri'nde 1990–2016 Yılları arasında gerçekleşen alansal değişimler. In Proceedings of the TUCAUM 2016 International Geography Symposium Book of Proceedings, Ankara, Turkey, 13–14 October 2016.

38. Sentinel Application Platform (SNAP). Available online: http://step.esa.int/main/toolboxes/snap (accessed on 20 December 2018).

39. Miranda, N. *Sentinel-1 Instrument Processing Facility: Impact of the Elevation Antenna Pattern Phase Compensation on the Interferometric Phase Preservation*; Technical Report, ESA-EOPG-CSCOP-TN-0004; European Space Agency: Paris, France, 2015.

40. Sentinel-1 Quality Control. Available online: https://qc.sentinel1.eo.esa.int (accessed on 20 December 2018).

41. Farr, T.G.; Rosen, P.A.; Caro, E.; Crippen, R.; Duren, R.; Hensley, S.; Alsdorf, D. The shuttle radar topography mission. *Rev. Geophys.* **2007**, *45*. [CrossRef]

42. Hooper, A.; Zebker, H.; Segall, P.; Kampes, B. A new method for measuring deformation on volcanoes and other natural terrains using InSAR persistent scatterers. *Geophys. Res. Lett.* **2004**, *31*, 5. [CrossRef]

43. Ferretti, A.; Prati, C.; Rocca, F. Permanent scatterers in SAR interferometry. *IEEE Transact. on Geoscie. Remote Sens.* **2001**, *39*, 8–20. [CrossRef]

44. Bekaert, D.P.S.; Walters, R.J.; Wright, T.J.; Hooper, A.J.; Parker, D.J. Statistical comparison of InSAR tropospheric correction techniques. *Remote Sens. Environ.* **2015**, *170*, 40–47. [CrossRef]

45. Wright, T.J.; Parsons, B.E.; Zhong, L. Toward mapping surface deformation in three dimensions using InSAR. *Geophys. Res. Lett.* **2004**, *31*, 169–178. [CrossRef]

46. Hu, J.; Li, Z.W.; Ding, X.L.; Zhu, J.J.; Zhang, L.; Sun, Q. Resolving three-dimensional surface displacements from InSAR measurements: A review. *Earth Sci. Rev.* **2014**, *133*, 1–17. [CrossRef]

47. Hürriyet Gazetesi. Available online: http://www.hurriyet.com.tr/gundem/eber-golu-tamamen-kurudu-40991682 (accessed on 2 January 2019).

48. T24 Bağımsız İnternet Gazetesi. Available online: http://t24.com.tr/haber/afyonkarahisardaki-eber-golu-tamamen-kurudu,727012 (accessed on 2 January 2019).

49. Winter, T.C.; Harvey, J.W.; Franke, O.L.; Alley, W.M. *Ground Water and Surface Water—A Single Resource*; Circular 1139; US Geological Survey: Reston, VA, USA, 1998.

50. Sophocleous, M. Interactions between groundwater and surface water: the state of the science. *Hydrogeol. J.* **2002**, *10*, 52–67. [CrossRef]

51. Ghoubachi, S.Y. Impact of lake Nasser on the groundwater of the Nubia sandstone aquifer system in Tushka area, South Western Desert, Egypt. *J. King Saud Univ. Sci.* **2012**, *24*, 101–109. [CrossRef]

52. Tezcan, L.; Meriç, B.T.; Doğdu, N.; Akan, B.; Atilla, A.Ö.; Kurttaş, T. *Akarçay havzası hidrojeolojisi ve yeraltısuyu akım modeli*; Project Final Report; Hacettepe University International Karst Water Sources Research and Application Center (UKAM): Valencia, CA, USA, 2002; p. 13.

53. The Turkish State Meteorological Service Web Site. Available online: https://www.mgm.gov.tr/veridegerlendirme/il-ve-ilceler-istatistik.aspx?k=A&m=AFYONKARAHISAR (accessed on 7 April 2019).

54. Bluedot Water Observatory. Available online: https://water.blue-dot-observatory.com/2361 (accessed on 19 November 2018).